HHS Public Access

Author manuscript

Sci Signal. Author manuscript; available in PMC 2019 October 30.

Published in final edited form as:

Sci Signal. ; 12(579): . doi:10.1126/scisignal.aav1439.

Loss of MCU prevents mitochondrial fusion in G1/S phase and blocks cell cycle progression and proliferation

Olha M. Koval[1], **Emily K. Nguyen**[1], **Velarchana Santhana**[1], **Trevor P. Fidler**[2,3], **Sara C. Sebag**[1], **Tyler P. Rasmussen**[1], **Dylan J. Mittauer**[1], **Stefan Strack**[4], **Prabhat C. Goswami**[5], **E. Dale Abel**[1,2], **Isabella M. Grumbach**[1,2,5,6,*]

[1]Abboud Cardiovascular Research Center, Division of Cardiovascular Medicine, Department of Internal Medicine, Carver College of Medicine, University of Iowa, Iowa City IA 52242, USA.

[2]Fraternal Order of Eagles Diabetes Research Center and Division of Endocrinology and Metabolism, Carver College of Medicine, University of Iowa, Iowa City, IA 52242, USA.

[3]Department of Molecular Medicine, Columbia University Medical Center, New York NY, 10032, USA.

[4]Department of Pharmacology, Carver College of Medicine, University of Iowa, Iowa City IA 52242, USA.

[5]Free Radical and Radiation Biology Program, Department of Radiation Oncology, Holden Comprehensive Cancer Center, University of Iowa, Iowa City IA 52242, USA.

[6]Veterans Affairs Healthcare System, Iowa City, IA 52246, USA.

Abstract

The role of the mitochondrial Ca^{2+} uniporter (MCU) in physiologic cell proliferation remains to be defined. Here, we demonstrated that the MCU was required to match mitochondrial function to metabolic demands during cell cycling. During the G1/S transition (the cycle phase with the highest mitochondrial ATP output), mitochondrial fusion, oxygen consumption and Ca^{2+} uptake increased in wild-type cells, but not in cells lacking MCU. In proliferating wild-type control cells, the addition of the growth factors promoted the activation of the Ca^{2+}/calmodulin-dependent kinase II (CaMKII) and the phosphorylation of the mitochondrial fission factor Drp1 at Ser^{616}. The lack of the MCU was associated with baseline activation of CaMKII, mitochondrial fragmentation due to increased Drp1 phosphorylation, and impaired mitochondrial respiration and glycolysis. The mitochondrial fission/fusion ratio and proliferation in MCU-deficient cells

*To whom correspondence should be addressed: isabella-grumbach@uiowa.edu.

AUTHOR CONTRBUTIONS

I.M.G. and O.M.K. designed the research. O.M.K. performed all Ca^{2+} imaging, bioenergetics experiments and most immunoblots, and also performed some microscopy experiments with help from E.K.N. E.K.N. performed additional immunoblots. V.S. performed the analysis of mitochondrial morphology and cell counts. T.P.F. performed the wounding experiments in mice. S.C.S. performed and analyzed histology experiments. T.P.R. performed cell culture experiments. D.J.M. performed the analysis of mitochondrial morphology, mitochondrial respiration and cell counts. P.C.G. helped with the cell cycle analysis. S.S. and E.D.A. provided critical reagents and scientific advice. I.M.G. and O.M.K. wrote the manuscript with input from the other authors.

COMPETING INTERESTS

The authors declare that they have no competing interests.

DATA AND MATERIALS AVAILABILITY

All data needed to evaluate the conclusions in the paper are present in the paper or the Supplementary Materials.

recovered after MCU restoration or inhibition of mitochondrial fragmentation or of CaMKII in the cytosol. Our data highlight a key function for the MCU in mitochondrial adaptation to the metabolic demands during cell cycle progression. Cytosolic CaMKII and the MCU participate in a regulatory circuit whereby mitochondrial Ca^{2+} uptake affects cell proliferation through Drp1.

INTRODUCTION

The mitochondrial Ca^{2+} uniporter (MCU) is a highly conserved protein of the inner mitochondrial membrane that mediates the electrophoretic Ca^{2+} uptake into the mitochondrial matrix (1, 2). MCU-dependent Ca^{2+} uptake increases TCA cycle activity by activating Ca^{2+}-dependent hydrogenases (3). Accordingly, MCU deficiency in cardiac muscle prevents the adaptation of energy supply to states of maximal demand (4). However, the role of MCU in less metabolically demanding physiologic processes such as cell proliferation remains unclear (5).

During the cell cycle, fluctuations in intracellular Ca^{2+} levels and transients occur (6) and drive the periodic activation of Ca^{2+}-sensitive regulators of proliferation such as Ca^{2+}/calmodulin (CaM), Ca^{2+}/CaM-dependent kinases (CaMK), and the phosphatase calcineurin (7, 8). Inhibition of mitochondrial Ca^{2+} uptake in proliferating smooth muscle cells disturbs cytosolic Ca^{2+} transients (9, 10). In a pancreatic beta-cell line, increased mitochondrial Ca^{2+} concentration in S and G2/M phase are associated with dynamic changes in cytosolic Ca^{2+} (11). Thus, because mitochondrial Ca^{2+} uptake contributes to the fluctuations in Ca^{2+} compartmentalization throughout the cell cycle (11), MCU may represent a fundamental but underappreciated regulator of cell cycle progression. *MCU*$^{-/-}$ mice at all ages have relatively lower body and organ weight compared to their wild type littermates, providing indirect evidence for a role of MCU in cell proliferation (12).

Dynamic changes in mitochondrial morphology promote early cell cycle progression (13) with mitochondria converting from a highly fragmented state in G0 to a hyper-fused network at G1/S transition. This event correlates with the high mitochondrial ATP output in cells that are otherwise predominantly dependent on glycolysis (13). The Ca^{2+}-dependent proliferation effectors CaMKI, CaMKII and CDK1, and calcineurin regulate mitochondrial fission mediated by the GTPase Drp1 (14–18). Altered cytosolic Ca^{2+} levels caused by decreased Ca^{2+} mitochondrial uptake are thus expected to promote fission mediated by Drp1, providing a potential mechanistic link for MCU-dependent proliferation. Here, we hypothesized that cell cycle progression requires coordination of mitochondrial and cytosolic Ca^{2+} levels and that MCU deficiency impairs cell proliferation by altering cytoplasmic Ca^{2+} transients, mitochondrial dynamics because of altered Drp1 phosphorylation, and mitochondrial energetics.

RESULTS

MCU deficiency decreases cell proliferation *in vivo and in vitro*.

Wound closure after cutaneous punch biopsy was significantly delayed in *MCU*$^{-/-}$ mice, with a 60% reduction in wound size compared to 85% in littermate wild type (WT) mice on

day 10 after injury (Fig. 1A, B). We also determined the area and number of cell nuclei in the aorta, an organ with limited postnatal proliferation, to test for developmental differences (Fig. 1C–E). H&E-staining of aortic cross-sections from 12- week old mice demonstrated a significant reduction in the area and number of nuclei in the medial layer in *MCU*$^{-/-}$ mice compared to WT littermates. The ratio of cells to area was similar in both genotypes, suggesting that the difference in size was at least partially driven by reduced cell numbers (Fig. 1F). To assess post-natal physiological organ regeneration, we labeled proliferating hepatocytes by PCNA immunostaining. Significantly fewer PCNA-positive cells were detected in liver sections from *MCU*$^{-/-}$ mice (fig. S1A, B). Together, these results implicate MCU as a regulator of cell proliferation. Moreover, as reported previously (12), male and female *MCU*$^{-/-}$ mice were significantly smaller than their WT littermates on postnatal days 18, 21 and 33 (fig. S1C–E). Although the weights of the spleen, heart, and kidney were significantly reduced in *MCU*$^{-/-}$ mice, the organ weight adjusted to total body weight was not different between genotypes, supporting a general effect of MCU deletion on organ development and growth (fig. S1F–H).

Acute silencing of MCU by siRNA or pharmacological inhibition with RU360 significantly reduced the number of WT vascular smooth muscle cells (VSMCs) in vitro at 72 h after treatment with platelet-derived growth factor (PDGF) (Fig. 1G, H), findings that were confirmed by cell counts of cultured skin fibroblasts from *MCU*$^{-/-}$ and WT mice (Fig. 1I). MCU inhibition reduces apoptotic cell death, making it unlikely that the detected differences in cell numbers result from increased apoptosis (12, 19). This notion was confirmed by TUNEL staining of VSMCs with MCU knockdown (Fig. 1J). Together, these data support that MCU deficiency reduces cell proliferation in fibroblasts and dedifferentiated smooth muscle cells.

MCU inhibition prolongs cytosolic Ca^{2+} transients.

MCU knockdown by siRNA (fig. S2A, B) decreased PDGF-induced mitochondrial Ca^{2+} transients, in particular the peak amplitude and the area under the curve (AUC), as measured using the mitochondrial Ca^{2+} indicator mtPericam (fig. S2C–E). These findings were recapitulated with MCU deletion or inhibition with RU360 (fig. S2F–H). The effects of MCU deficiency on cytoplasmic Ca^{2+} levels were evaluated by Fura-2AM imaging of proliferating VSMCs. Inhibition or knockout of MCU significantly increased the peak amplitude and AUC of cytosolic Ca^{2+} transients after PDGF treatment (Fig. 2A–C), suggesting higher peak concentrations and impaired clearance. The uptake of mitochondrial Ca^{2+} and its release after application of FCCP were reduced in *MCU*$^{-/-}$ skin fibroblasts (Fig. 2D). To determine ER Ca^{2+} content, WT and *MCU*$^{-/-}$ skin fibroblasts were treated with the SERCA inhibitor thapsigargin. The cytoplasmic Ca^{2+} transients in *MCU*$^{-/-}$ VSMCs were prolonged compared to WT (Fig. 2E, F). The Fura-2AM signal at baseline was similar between genotypes (Fig. 2G). Lastly, we recorded the cytoplasmic Ca^{2+} levels after PDGF administration over 50 min (3000 s, Fig. 2H). After the initial treatment, the cytosolic Ca2+ levels returned to baseline in WT, but not in MCU$^{-/-}$ VSMCs in which the repeated addition of PDGF further increased cytoplasmic Ca^{2+} levels. These data demonstrate that MCU inhibition prolongs cytosolic Ca^{2+} transients after PDGF treatment in VSMCs.

MCU is required to adapt mitochondrial ATP production to energy demands during the cell cycle.

We next sought to determine how MCU deletion affects cell cycle progression and analyzed WT or *MCU*$^{-/-}$ fibroblasts in growth arrest and at 16 and 24 h after release from arrest. At 16 h, 41% of WT fibroblasts had entered S phase compared to 18 % of *MCU*$^{-/-}$ cells (Fig. 3A, B) and cyclin D and E protein abundance significantly increased in WT but not in *MCU*$^{-/-}$ fibroblasts (Fig. 3C–E). To corroborate that MCU deletion impaired S phase entry, cells were arrested at the G1/S transition by incubation with Aphidicolin, an inhibitor of DNA polymerases. At 5 h after removal of Aphidicolin, significantly more WT than *MCU*$^{-/-}$ fibroblasts had entered S phase (Fig. 3F, G). We also confirmed these findings by assessing the cell cycle progression in WT and MCU$^{-/-}$ VSMCs (fig. S3A, B). Mitochondrial fusion occurs at the G1/S transition (13), and progression to S phase correlates with greater mitochondrial ATP production (11). As anticipated, mitochondria were predominantly fragmented in growth-arrested WT and *MCU*$^{-/-}$ fibroblasts (Fig. 3H, I). Whereas mitochondria in WT fibroblasts elongated within 16 h of exposure to growth factors, mitochondria in *MCU*$^{-/-}$ fibroblasts remained mostly fragmented.

Next, we investigated how MCU deletion affects cytosolic Ca^{2+} levels, and mitochondrial respiration. Cytosolic Ca^{2+} concentrations were significantly increased in WT fibroblasts at 16 h after release from growth arrest, but not in *MCU*$^{-/-}$ fibroblasts (Fig. 4A). Moreover, WT cells showed that mitochondrial Ca^{2+} uptake increased 16 h after release from growth arrest in parallel with a rise in oxygen consumption rate, but these changes did not occur in *MCU*$^{-/-}$ cells (Fig. 4B, C). Because mitochondrial fusion promotes mitochondrial Ca^{2+} uptake that fuels oxidative phosphorylation and mitochondrial ATP production (13), our data suggest that MCU is required to adapt mitochondrial ATP production to energy demands during the cell cycle. To test whether the expression of proteins in the MCU complex changes during the cell cycle, we performed immunoblots in mitochondria of WT and *MCU*$^{-/-}$ fibroblasts at 16 and 24 h after release from cell cycle arrest (Fig. 4D). The protein levels of the regulatory subunits MCUB and EMRE at 16 h were reduced compared to those at 0 and 24 h and the levels of NCLX and MICU1 at 16 h were lower than those at 0 h (Fig. 4F–H). MCU deletion led to loss of EMRE, reduced levels of NCLX and attenuated the changes throughout the cell cycle (Fig. 4D). These data suggest that the dynamic regulation of the MCU complex during the cell cycle leads to increased mitochondrial Ca^{2+} uptake in S phase in parallel to mitochondrial fusion and increased mitochondrial respiration.

MCU affects mitochondrial dynamics.

Mitochondrial fission and fusion are controlled by GTPases, including Drp1, a key regulator of mitochondrial fission at the outer mitochondrial membrane (20). Drp1 is regulated by phosphorylation, which is partially controlled by Ca^{2+}-dependent signaling (14–16). The phosphorylation of Drp1 at Ser^{616} promotes mitochondrial fragmentation (18). Because we detected mitochondrial fission in MCU-inhibited cells, we hypothesized that these findings were due to increased Drp1 phosphorylation. As anticipated, acute PDGF treatment induced Drp1 phosphorylation at Ser^{616} in proliferating WT VSMCs (Fig. 5A, B). However, VSMCs with MCU knockdown displayed high baseline Drp1 phosphorylation that did not further increase with PDGF. Accordingly, mitochondrial fission was induced by PDGF in

proliferating control cells, but not in VSMCs with MCU knockdown that displayed fragmented mitochondria at baseline (fig. S4A, B). These findings were recapitulated in vivo. Baseline Drp1 phosphorylation was significantly higher in the heart and aorta of *MCU* $^{-/-}$ mice (Fig. 5C, D). Once activated, Drp1 associates with the outer mitochondrial membrane (16). Accordingly, at baseline, significantly more Drp1 associated with mitochondria in MCU knockdown cells than in WT cells (Fig. 5E, F). In response to PDGF, co-localization of Drp1 with mitochondria increased in WT cells, but not in MCU-deficient cells.

Drp1 and its phosphorylation by CaMKII are required to inhibit proliferation in MCU-deficient cells.

To dissect whether Drp1 regulates the proliferation defect in *MCU*$^{-/-}$ cells, *Drp1*$^{-/-}$ fibroblasts with MCU knockdown or overexpression were used. Drp1 deletion alone significantly reduced the number of proliferating cells; however, gain or loss of MCU expression did not affect cell numbers beyond those observed after Drp1 knockout (Fig. 5G–I). These data demonstrate that the presence of Drp1 is required for the effects of MCU on cell proliferation. Several kinases including PKC, CDK1, and CaMKII promote the phosphorylation of Drp1 at Ser^{616} (14–16, 21). A screen for PKC phosphorylation targets showed no increased PKC activity in tissue samples of *MCU*$^{-/-}$ mice (fig. S5). However, increased CaMKII activation by autophosphorylation was detected in *MCU*$^{-/-}$ VSMCs at baseline (Fig. 6A, B) which did not further increase after PDGF treatment. In contrast, in WT VSMCs, PDGF induced a robust activation of CaMKII. In parallel to the association of Drp1 with mitochondria upon PDGF treatment in WT cells, more CaMKII was detected in mitochondrial fractions at 30 min after addition of PDGF (fig. S6A–C). Consistent with in vitro data, CaMKII activation was higher in the skin and aorta of *MCU*$^{-/-}$ mice than in those from WT mice (Fig. 6C, D). Treatment of WT VSMCs with the CaMKII inhibitor KN93 significantly decreased Drp1 phosphorylation in response to PDGF, suggesting a link between CaMKII activity and Drp1 phosphorylation (Fig. 6E, F). Overexpression of the dominant negative CaMKII T287A mutant which is missing a functional autophosphorylation site promoted mitochondrial fusion in cells of both genotypes at baseline and restored PDGF-induced fission in *MCU*$^{-/-}$ VSMCs, demonstrating that alterations in mitochondrial fission are due to CaMKII-driven Drp1 phosphorylation (Fig. 6G, H). Similarly, CaMKII inhibition by adenoviral overexpression of the potent and specific CaMKII inhibitor peptide CaMKIIN (22) normalized Drp1 phosphorylation at baseline and restored PDGF-induced Drp1 phosphorylation and mitochondrial fission only in *MCU*$^{-/-}$ cells (Fig. 6I–L).

MCU is necessary to maintain mitochondrial reserve capacity in VSMCs.

Mitochondrial Ca^{2+} uptake through MCU fuels ETC protein activity and is necessary to maintain mitochondrial reserve capacity in cardiac myocytes (12). We tested whether this is also true in proliferating VSMCs. First, we established that baseline and reserve respiration and extracellular acidification rate (ECAR) were impaired in *MCU*$^{-/-}$ cells under growth conditions (Fig. 7A–C). CaMKII inhibition restored respiration and lactate production in *MCU*$^{-/-}$ VSMCs, but not in WT cells (Fig. 7D–G). Lastly, we established that cytosolic

CaMKII inhibition restored proliferation of MCU deficient VSMCs while decreasing proliferation in WT cells (Fig. 7H).

Inhibition of PKC by Go6083 had no effect on respiration in both genotypes (fig. S7A, B). Because we used cells with a constitutive MCU deletion, these findings could be due to adaptation to constitutive MCU deletion as opposed to MCU deficiency. Thus, we also measured mitochondrial bioenergetics in VSMCs with acute MCU knockdown, which confirmed the findings in *MCU*$^{-/-}$ VSMCs (fig. S8A–F). Moreover, overexpression of MCU in *MCU*$^{-/-}$ cells increased mitochondrial Ca^{2+} uptake (fig. S9A), decreased baseline Drp1 phosphorylation and mitochondrial fission and restored the response to PDGF (fig. S9B–D). MCU overexpression improved mitochondrial respiration and ECAR in *MCU*$^{-/-}$ cells, but not in WT cells (fig. S9E, F). To test whether the inhibitory effect of MCU deletion on mitochondrial respiration was due to exaggerated mitochondrial fragmentation, we blocked mitochondrial fission with the Drp1 inhibitor peptide P110. P110 specifically inhibits the interaction of Drp1 with Fis1 (23). P110 delivery improved mitochondrial respiration in *MCU*$^{-/-}$ VSMCs after PDGF treatment and restored mitochondrial fusion at baseline and fission in response to PDGF (Fig. 8A–D). The inhibition of mitochondrial fission also increased mitochondrial Ca^{2+} uptake in WT and in *MCU*$^{-/-}$ cells (Fig. 8E). In WT VSMCs, overexpression of a constitutively active mutant of CaMKII (CaMKII T287D) induced mitochondrial fission and abrogated further fragmentation by PDGF, whereas P110 pretreatment of WT cells abrogated fission by PDGF (Fig. 8F). When overexpression of constitutively active CaMKII and Drp1 inhibition with P110 were combined, increased mitochondrial fusion at baseline but increased fission following PDGF treatment was observed, substantiating that cytosolic CaMKII is upstream of endogenous Drp1 and enhances mitochondrial fission through Drp1. Overexpression of OPA1 and MFN1/2, which drive mitochondrial fusion at the inner and outer mitochondrial membranes, increased the mitochondrial form factor at baseline in WT and *MCU*$^{-/-}$ VSMCs. However, in contrast to the DRP1 inhibitor P110, OPA1 and MFN1/2 overexpression in *MCU*$^{-/-}$ VSMCs did not recover mitochondrial fission following PDGF treatment (Fig. 8G–I), corroborating that the effects of MCU deletion are through Drp1 activation (Fig. 8J).

DISCUSSION

Here, we demonstrated that MCU deficiency inhibited proliferation in wound healing, organ development and postnatal tissue homeostasis in vivo and of smooth muscle and fibroblasts in vitro. In MCU-deficient cells, cell cycle progression was delayed at the G1/S transition, a stage in WT cells characterized by mitochondrial fusion and increased mitochondrial Ca^{2+} uptake. MCU deficiency delayed cytosolic Ca^{2+} clearance after ER Ca^{2+} release, increased activation of CaMKII, Drp1 phosphorylation at Ser^{616}, mitochondrial fission, impaired mitochondrial respiration and glycolysis and cell proliferation. Mitochondrial OCR and cell proliferation were restored by either MCU overexpression or inhibition of mitochondrial fission or of cytosolic CaMKII in MCU-deficient but not in WT cells. Thus, we posit that Drp1 phosphorylation occurs physiologically in response to growth factor treatment of WT cells secondary to transient activation of CaMKII. When MCU is absent, constitutive activation of CaMKII promotes constitutive fission, which prevents a subsequent fusion event that is required for cell cycle progression (Fig. 8J). By controlling cytosolic Ca^{2+}

transients and Ca^{2+}-dependent signaling mediated by CaMKII, MCU regulates mitochondrial dynamics in G1/S phase and respiration necessary for cell cycle progression.

Although the decreased body weight of *MCU*$^{-/-}$ mice suggests impaired cell proliferation (12), current data on MCU as a regulator of cell proliferation are limited to cancer cell lines. MCU expression has been positively correlated with poor prognosis, tumor cell migration, invasion, and resistance to apoptosis, but not to cell proliferation (24–27). These results may not adequately be representative Ca^{2+} regulation during cell proliferation in non-malignant cells because oncogene activation alters relevant Ca^{2+} signaling (28). Changes in the expression or function of Orai3 in breast (29) and SERCA in prostate cancer (30) imply that cytosolic Ca^{2+} fluxes are altered at various points during the cell cycle. Nonetheless, inhibition of the leucine zipper/EF hand-containing transmembrane-1 protein (LETM1), which promotes mitochondrial Ca^{2+} influx and efflux, impaired fibroblasts proliferation, although the underlying mechanism remains unclear (31).

At G1/S transition, mitochondria are hyperfused and have increased capacity to take up Ca^{2+} through MCU (6, 11, 13). Here, we demonstrated that MCU was required to maintain cell cycle progression, cytosolic Ca^{2+} clearance and mitochondrial hyperfusion during G1/S phase (Fig. 3A, B, H, I and 4A, B). The mechanisms behind mitochondrial hyperfusion in G1/S transition (13) are not clear. Hyperfusion could be caused by inhibition of Drp1, for example by dephosphorylation at Ser^{616} (11) or activation of fusion proteins like Mfn1/2. Our findings that cytosolic Ca^{2+} levels increase in WT cells at G1/S (Fig. 4A) imply that mechanisms in addition to Drp1 Ser^{616} dephosphorylation are in place at this stage. MCU deletion leads to excessive activation of Ca^{2+}/CaMKII/Drp1-dependent fission and thus disrupts these mechanisms. However, we also cannot exclude that other Ca^{2+}-dependent regulators of mitochondrial fission such as calcineurin contribute to the phenotype of *MCU*$^{-/-}$ cells (16). Cytosolic CaMKII was activated even in the absence of Ca^{2+}-mobilizing growth factors in MCU deficient cells. Autophosphorylation of CaMKII at Thr^{287} after an initial Ca^{2+}/CaM burst prevents rebinding of the autoinhibitory segment to the kinase and is the key event by which CaMKII gains Ca^{2+}-independence (32). In MCU-deficient cells, cytosolic Ca^{2+} clearance was delayed after growth factor application over a prolonged time period (Fig. 2H). Minor differences in baseline cytoplasmic Ca^{2+} levels were seen as previously reported (10). The delayed cytosolic Ca^{2+} clearance without increased baseline levels may be sufficient to sustain CaMKII activity and Drp1 Ser^{616} phosphorylation. CaMKII has been identified as cell cycle promoter, for example by activating CDC25 in G2 phase (33). CaMKII inhibition in MCU-deficient cells restored PDGF-dependent Drp1 phosphorylation. We posit that this occurs through activation of other kinases that target Drp1 Ser^{616}, such as Erk1/2, CDK1 or the Ca^{2+}-independent PKC isoform d (17). Moreover, mitochondrial OCR increased with CaMKII inhibition even in the absence of MCU, consistent with reports of higher mitochondrial cristae number and ATP synthesis activity in cells with hyperfused, tubular mitochondria (34, 35). By contrast, PKCd inhibition or overexpression of Opa1 and Mfn1/2 did not rescue metabolism or mitochondrial dynamics in MCU-deficient cells (fig. S7A, B and Fig. 8H), supporting that mitochondrial fission and its downstream effects are indeed driven by altered cytosolic Ca^{2+} levels.

Although numerous cytosolic regulators of mitochondrial dynamics during mitosis have been identified, our data imply that mitochondria through MCU-dependent Ca^{2+} influx modulate mitochondrial fission and thereby cell proliferation. The MCU complex subunits MICU, EMRE and MCUb regulate MCU activity (36–38) and the complex composition determines the diverse MCU activity in different tissues (39). In our experiments, we detected evidence for changes in MCU subunit composition that coincided with increased mitochondrial Ca^{2+} uptake in G1/S phase. In particular, the negative MCU regulator MCUB (37) and the subunit EMRE that is required for opening of the MCU pore and its tight regulation by MICU (40, 41) as well MICU1 (42) were affected. Thus, it is tempting to speculate that acute changes in MCU subunit composition or activity during the cell cycle affect mitochondrial Ca^{2+} uptake, which positions the MCU complex as an active regulator of cell cycle progression and cell proliferation. Further experiments to ascertain the complex composition in the inner mitochondrial membrane and investigations into the regulation of these events will be necessary to corroborate the role of the MCU complex in this context.

MATERIALS AND METHODS

Animals

All animal procedures were approved by the University of Iowa Institutional Animal Care and Use Committee protocol. This study was carried out in strict accordance with the recommendations in the Guide for the Care and Use of Laboratory Animals of the National Institutes of Health. We used 10–16-week old male and female *MCU*$^{-/-}$ mice, a kind gift from Dr. Toren Finkel, NIH, in CD1 background and littermate controls on regular chow (Teklad, 7913) for all in vivo experiments. The body weight in *MCU*$^{-/-}$ mice and their littermates were determined on postnatal days 7, 18, 21, and 28 and before euthanasia. Weights of the heart, liver, and kidneys were obtained after euthanasia and expressed as ratios of organ to body weight.

Skin wounding

Mice were anesthetized with isoflurane. To create full-thickness skin wounds, mice were shaved and surgical scrub was performed at the surgical site. A sterile 6-mm biopsy punch was placed on the back and a punch of dorso-rostral back skin and panniculus carnosum was excised. Care was taken not to injure underlying muscles. Digital photographs were acquired on the day of surgery and every day thereafter. The wound margins were traced in Image J to calculate the wound area (43).

Histology and sectioning

The aortas and livers from 12-week old *MCU*$^{-/-}$ and WT littermates were fixed in 4% paraformaldehyde and embedded in paraffin. Five-micrometer sections of the aorta and liver were collected on Superfrost™ Plus slides. H&E-staining was performed on sections of the distal thoracic aorta. Deparaffinized liver sections were washed with PBS and permeabilized with 0.1% Triton X-100 solution for 10 min at room temperature and blocked with the Vector® M.O.M® Detection kit (Vector Laboratories). Anti-PCNA primary antibody was applied for 1 h at room temperature. Sections were washed with PBS before application of

an HRP-conjugated secondary antibody for 30 min. DAB was then applied for 10 min. Finally, the sections were counterstained with Harris hematoxylin for 10 s.

Cell isolation and culture

Mouse aortic smooth muscle cells (VSMCs) were isolated from male and female mice by enzymatic dispersion (44). Cells were cultured in low glucose (1mM) DMEM with pyruvate supplemented with 10% fetal bovine serum (FBS), 100 U/mL penicillin, 100 μg/mL streptomycin, 8 mM HEPES, MEM vitamins, and non-essential amino acids at 37°C in a humidified 95% air and 5% CO_2 incubator. Passage-matched mouse VSMCs from 5 to 10 passages were used for all experiments. Skin fibroblasts were isolated from 1-week old male and female $MCU^{-/-}$ and WT littermate mouse pups. (45). After removal of the epidermis, the dermis was cut into small pieces under sterile conditions and digested overnight in DMEM with Fungizone and antibiotics with 300 U/mL collagenase type I. The following day, the digested material was dispersed by vigorous pipetting and centrifuged at 1200 rpm for 5 min. The pelleted cells were plated in DMEM supplemented with 10% FBS, penicillin/streptomycin and Fungizone 2.5 μg/mL. Cells from passages 1–5 were used.

siRNA transfection

Five hundred thousand VSMCs were seeded in a T75 flask overnight. The next day, small interfering RNA (siRNA) duplexes for MCU (5' – CGACCUAGAGAAAUACAAUCAGCTC – 3' and 5' – GGGAAUAAAGGGAUCUUAAAUGCTG – 3 at a 1:1 ratio) or scramble control (5' – CGUUAAUCGCGUAUAAUACGCGUA – 3', Integrated DNA Technologies) were transfected (5 nM in 20 μl DharmaFECT 4 reagent). Knockdown efficiency was determined after 72 h by western blotting for MCU which was normalized to COXIV signal. The knockdown efficiency was consistently greater than 75%.

Cell counting

VSMCs and skin fibroblasts were cultured in 12-well plates at 5,000 cells per well in 2 mL DMEM containing 10% FBS. Twenty-four hours after plating, cells were treated with PDGF (20 ng/mL). RU360 (100 nM) was added with PDGF to some wells. After 24–72 h, cells were trypsinized and counted in triplicate using a Beckman Coulter Z1 cell counter.

TUNEL staining

VSMCs were plated onto 8-chamber microscopy slides. Apoptosis was induced by starvation in serum-free DMEM. After 48 h, VSMCs were fixed in 4% paraformaldehyde, then permeabilized with 0.1% Triton X-100 for 10 min. TUNEL staining was performed with a TUNEL staining kit (Roche) and mounted in Vectashield® mounting medium with propidium iodide. Ten fields per well were analyzed at 20X using a Zeiss LSM 510 microscope. Data are presented as a percent of TUNEL positive nuclei to total number.

Cytosolic Ca^{2+} imaging

Cells cultured on glass-bottomed tissue culture dishes were washed once with Normal Tyrode's buffer and incubated with 2.5 μM Fura-2AM (Invitrogen) in loading buffer with

2% BSA for 20 min at room temperature. Cells were then washed twice with Normal Tyrode's buffer and incubated for another 10 min at 37°C to allow for de-esterification of Fura-2AM. To record the changes in cytosolic Ca^{2+} transients, images were acquired continuously, from 3 min before and at least 10 min after PDGF treatment using an Olympus IX81 Inverted Light microscope. The cells were excited alternatively at 340 and 380 nm. Fluorescence signal intensity was acquired at 510 nm. Data are presented as AUC and peak amplitude. To estimate baseline cytoplasmic Ca^{2+} levels, two adjacent chambers were created on a glass bottom microwell dish by applying a divider of vacuum grease. Then, VSMCs transfected with MCU siRNA or scrambled control were seeded in the two chambers without mixing the two cell preparations. Fura 2-AM imaging was performed as described above.

Ca^{2+} retention assay

Calcium green-5N was used to monitor extramitochondrial Ca^{2+} in digitonin-permeabilized cultured skin fibroblasts. Recordings of mitochondrial Ca^{2+} uptake were performed in a 96-well plate with 100 μl of respiration buffer (100 mM K Aspartate, 20 mM KCl, 10 mM HEPES, 5 mM glutamate, 5 mM malate and 5 mM succinate pH 7.3) supplemented with 100 μM blebbistatin, 5 μM thapsigargin, 0.005% digitonin and 1 μM Calcium green-5N (Invitrogen). Calcium green-5N fluorescence was monitored at 485 nm excitation; 535 nm emission, after adding $CaCl_2$ (100 μM free Ca^{2+} at 30 °C). FCCP was added at a concentration of 25 μM.

Adenoviral transduction

Recombination and amplification of adenoviruses expressing CaMKIIN (Ad-CaMKIIN), constitutively active CaMKII (Ad-CaMKIIT287D), mitochondrial targeted EGFP (Ad-mtGFP), mitochondrial targeted Pericam (Ad-mtPericam) or empty (Ad-control) were performed by the Gene Transfer Vector Core at the University of Iowa. VSMC were incubated with adenoviruses at a multiplicity of infection (MOI) of 50 in serum-free media overnight. Subsequent experiments were conducted 48–72 h after adenoviral transduction (46).

Nucleofection

VSCMs were transfected in a NucleofectorTM I device (Lonza) with the Basic NucleofectorTM Kit for Primary Mammalian Smooth Muscle Cells (Lonza #VPI-1004), following the manufacturer's protocol. 600, 000 cells were transfected in the presence of 5 μg plasmid DNA, plated onto 35 mm glass bottom microwell dishes (MatTek Corporation) and grown for 72 h before experiments were performed.

Mitochondrial Ca^{2+} imaging

Cells previously transfected with siRNAs for 72–96 h were seeded onto 35 mm glass bottom microwell dishes (MatTek Corporation), infected with mt-Pericam adenovirus and incubated for 48 h. Pericam fluorescence was determined in cells in Tyrode's solution (140 mM NaCl, 10 mM Glucose, 5.4 mM KCl, 1.8 mM $CaCl_2$, 2.0 mM $MgCl_2$, 1.2 mM KH_2PO_4, 5 mM HEPES, pH 7.4 with NaOH). Imaging was performed at room temperature with a Leica TCS

SP8 STED confocal microscope. Pericam was excited at 405 nm and 480 nm and its emission recorded at 535 nm. ATP (100 μM) or PDGF (20 ng/mL) were added by micropipet (in 10 μL amounts) to trigger mitochondrial Ca^{2+} uptake. Recordings were performed every 5 s for at least 10 min. Mt-Pericam signals were quantified by ImageJ. The rise in amplitude above baseline and the area under the curve for 5 min after PDGF application were calculated. Peak amplitude (R) was calculated using $R_{peak} - R_{baseline}$. The area under the curve (AUC) was determined by subtracting the AUC at the baseline ratio. Summary data represent the average difference in basal and peak mitochondrial [Ca^{2+}].

Cell cycle analysis

VSMCs transfected with MCU siRNA or scramble or WT and *MCU*$^{-/-}$ skin fibroblasts were grown to confluence and maintained in a post-confluent state for 48 h, and then split to 50% density. DMEM with 10% FBS was added for the indicated times (24 and 32 h for VSMCs and 16 h and 24 h for skin fibroblasts). For some experiments, treatment with Aphidicolin (2μg/ml) for 24 h was used to arrest skin fibroblasts at the G1/S cell cycle transition. After 24 h, cells were washed with PBS and cultured in DMEM with 10% FBS and PDGF (20 ng/mL) for 5 h. The cells were harvested, fixed with 75% ice cold ethanol, and stained with propidium iodide (stock solution 50 μg/mL) and analyzed in a LSRII Flow Cytometer (Becton Dickinson).

Cell lysis and fractionation

For whole cell lysates, cells were lysed in RIPA buffer (20 mM Tris, 150 mM NaCl, 5 mM EDTA, 5 mM EGTA, 1% Triton X-100, 0.5% deoxycholate, 0.1% SDS, pH 7.4) supplemented with protease (Mini cOmplete, Roche) and phosphatase inhibitors (PhosSTOP, Roche). Lysates were sonicated and debris pelleted by centrifugation at 10,000× *g* for 10 min at 4°C. For mitochondrial fraction preparation, cells were washed in PBS and in MSEM buffer (5 mM MOPS, 70 mM sucrose, 2 mM EGTA, 220 mM Mannitol, pH 7.5 with protease inhibitors) prior to homogenization in cold MSEM buffer using 50 strokes in a Potter-Elvehjem glass Teflon homogenizer. Nuclei and cell debris were pelleted by centrifugation at 600 × *g* for 5 min at 4°C. Mitochondria were separated from the cytosolic fraction by centrifugation at 8000 × *g* for 10 min at 4°C. Protein concentrations were determined by Pierce™ BCA protein assay (Thermo Scientific).

Immunoblotting

Equivalent amounts of protein (5–15 μg) of were separated on NuPAGE 4–12% Bis-Tris gels (Life Technologies) and transferred to polyvinyl difluoride (PVDF) membranes (BioRad). Membranes were blocked in 5% BSA and incubated overnight at 4°C with primary antibodies. Blots were washed 3 times for 10 minutes with 0.05% Tween-20 in TBS and incubated for 1 h at room temperature with the secondary antibodies at a dilution of 1:5000 to 1:15,000. Blots were developed with ECL chemiluminescent substrate, scanned and analyzed using ImageJ software.

Confocal microscopy

For immunofluorescence imaging, cells were grown on coverslips pre-coated with 0.1% gelatin. Mitochondria were labeled by transduction with adenovirus expressing mitoGFP for 48 h or loading with 200 nM MitoTracker-Deep Red at 37°C for 30 min, fixed in 4% paraformaldehyde and permeabilized with 0.1% Triton X-100 in PBS. Cells were blocked in blocking buffer (1x PBS with 2% glycerol, 50 mM ammonium chloride, 5% fetal bovine serum, and 2% goat serum). Rabbit anti-Drp1 antibody was applied at 1:100 in blocking buffer overnight at 4°C. After rinsing three times in PBS, goat anti-rabbit secondary antibody (1:2000, Alexa Fluor568) was applied for 1 h at room temperature. Cells were mounted in Vectashield® mounting medium with DAPI. Images were acquired using a Zeiss LSM510 confocal microscope equipped with a 63× oil-immersion objective, excited with an argon laser at 488 nm filtered with NFT490 and BP505–530 Zeiss filters and HeNe laser at 543 (NFT565/BP575–615) and controlled by ZEN software (Zeiss). Colocalization of Drp1 with mitochondria was quantified as the Pearson's coefficient using the JaCoP plug-in for NIH ImageJ software.

Mitochondrial morphology quantification

Mitochondrial fission and fusion were determined in VSMCs transduced with adenovirus expressing mtGFP (MOI 50) for 48 hr. For automated morphometry, images were processed using NIH ImageJ software with the plugins involving either "rolling ball" background subtraction or deblurring by 2-D deconvolution with a computed point spread function. Using a custom-written NIH ImageJ macro provided by Dr. Stefan Strack (University of Iowa), processed images were converted to binary (black and white) images by auto-thresholding, and mitochondrial particles were analyzed for length or form factor (perimeter $2/(4 \times \pi \times \text{area})$ (47, 48). The parameters for form factor are set with minimum value of 1 for perfectly circular mitochondria.

Assessment of bioenergetics

OCR was monitored with an ESA BioStat Multi Electrode System (ESA Products, Dionex Corp) in conjunction with a YSI Oxygen Probe (5331) and glass reaction chamber vials in a YSI bath assembly (5301) (Yellow Springs Instruments), all at room temperature. Cells were suspended in HBSS media at a density of ($1–3 \times 10^6$) cells per 1 mL; the typical sample size was 2.00 mL. For experiments in the Seahorse XF Analyzer, VSMCs were plated onto 96-well Seahorse plate at a density of 20,000 per well 24 h before the experiment. The cells were equilibrated in Seahorse assay medium (unbuffered DMEM) for 1 h. PDGF (20 ng/mL) was added immediately before the assay in a Seahorse Bioscience XF96 analyzer. Oligomycin, FCCP, and antimycin/rotenone were added to some wells at concentrations of 1, 1.5, and 2 μM respectively. Total ATP, ADP, and AMP were determined with the AMP-Glo kit (Promega Corporation, V5011) in 10 μg total cell lysates. All measurements were performed in triplicates. Lactate levels were measured with the Lactate Analyzer (Lactate Scout, EKF Diagnostics) with Lactate Scout Test Strips (Code 55). A standard curve was established from 0.5 to 5 mM with sodium lactate in cell culture medium with 10% FBS. Skin fibroblasts were grown to 90% confluency, serum-starved for 24 h and then, grown in

medium with 10% FBS for 16 h. Cells were trypsinized, counted, and lysed in hypotonic lysis buffer. Lactate concentrations were normalized to cell numbers.

P110 peptide delivery

Chariot ™ was used for intracellular delivery of the peptide P110 (synthesized by GenScript) based on the manufacturer's protocol. The transfection mixture of 100 μL Opti-MEM, 5 μL Chariot, and P110 (2 mM)) were mixed and incubated at room temperature for 30 min and then added to VSMCs in a final volume of 1mL for 1 h hour before the experiment.

Materials

The following reagents were purchased from Thermo Fisher Scientific: Thapsigargin (T7459), Recombinant Mouse Platelet Derived Growth Factor-BB (PDGF-BB, PMG0044), MitoSOX-Red (M36008), DharmaFECT 4 reagent (T-2004–02) and Fura-2AM (F1221). The TUNEL staining kit (#12156792910) was bought from Roche. Aphidicolin was purchased from Sigma (A4487). To increase intracellular Ca^{2+}, we applied ATP (Research Product Internation Corp, A300030) and Caffeine (Sigma-Aldrich, #C0750). RU360 (Calbiochem #557440) was applied as a pharmacological inhibitor of MCU. To visualize mitochondria or the mitochondrial membrane potential, we used MitoTracker- Deep Red (Life Technology, M22426) or TMRM (Invitrogen, I34361) respectively. The Drp1 inhibitor peptide P110 – TAT was synthesized by GenScript and delivered with the protein delivery reagent Chariot ™ from Active Motif (#30025). Mouse-on-mouse (MOM) and Vectashield kits with DAPI or propidium iodide were purchased from Vectors Laboratories. The water-soluble CaMKII inhibitor KN-93 was purchased from Calbiochem/EMD Millipore (422711). For dissociation of the skin or aorta, Collagenase type II (4174) and collagenase type I (4194) from Worthington Biochemical Corporation were used. The anti-CaMKII antibody used for western blots was purchased from EMD Millipore (N-terminus, #07–1496). Anti-phospho CaMKII (Thr^{287}, #12716), anti-phospho pDRP-1 (Ser^{616}, D9A1, #4494), anti-DRP1 (D6C7, #8570), anti-Cyclin D (#2229S), anti-CoxIV (#4850S), anti-GAPDH (#2178), anti-pSer PKC phosphorylation targets (#2261) and anti-mouse IgG-HRP (#7076S) antibodies were purchased from Cell Signaling Technology. Anti-rabbit IgG-HRP (#1706515) was acquired from BioRad, anti-MCUA antibody (Prestige Antibodies, HPA016480), anti-EMRE (HPA060340), anti-NCLX (SAB2102181) and anti-MICU1 (HPA037480) were purchased from Sigma. Anti-MCUB was purchased from Abgent (C109B, AP12355b). Anti-proliferating cell nuclear antigen (PCNA) monoclonal antibody was from Invitrogen (13–3900). Anti-cyclin E (sc-481) and the ECL reagent were purchased from Santa Cruz Biotechnology (sc-2048).

Statistical analysis

All data are presented as means ± standard error of the mean (SEM). Normal distribution was established by D'Agostino-Pearson omnibus normality test. Differences within and between groups were tested for significance by One-way analysis of variance (ANOVA) followed by the Tukey post-hoc test or by an unpaired t-test (GraphPad Prism 7.0). For paired samples, an analysis by Wilcoxon matched-pairs signed rank test was performed. Repeat measure 2-way ANOVA was performed for growth curves and measurements of

wound size. When normal distribution was absent, a Kruskal-Wallis or Mann-Whitney test was performed. A p-value of less than 0.05 was considered statistically significant.

Supplementary Material

Refer to Web version on PubMed Central for supplementary material.

ACKNOWLEDGMENTS

We thank Dr. Colette Galet for her editorial assistance, Dr. Johannes Ledolter for consulting on biostatistical analyses and Dr. Toren Finkel for $MCU^{-/-}$ mice.

FUNDING

The project was supported by grants from the NIH (R01 HL 108932 to IMG, R01 HL127764 and R01 HL112413 to EDA, R01 DK11662 to SS, R01 CA111365 to PG, and TL1-TR-001875 to TPF); the Veterans Affairs Iowa City (I01 BX000163 to IMG), the American Heart Association (17GRNT33660032 to IMG) and from the NIH NHLBI (F30 HL131078, T32 GM007337 to EKN).

REFERENCES AND NOTES

1. Baughman JM et al., Integrative genomics identifies MCU as an essential component of the mitochondrial calcium uniporter. Nature 476, 341–345 (2011). [PubMed: 21685886]
2. De Stefani D, Raffaello A, Teardo E, Szabo I, Rizzuto R, A forty-kilodalton protein of the inner membrane is the mitochondrial calcium uniporter. Nature 476, 336–340 (2011). [PubMed: 21685888]
3. Ezawa I, Ogata E, Ca2+-induced activation of succinate dehydrogenase and the regulation of mitochondrial oxidative reactions. J Biochem 85, 65–74 (1979). [PubMed: 762052]
4. Wu Y et al., The mitochondrial uniporter controls fight or flight heart rate increases. Nat Commun 6, 6081 (2015). [PubMed: 25603276]
5. Kamer KJ, Mootha VK, The molecular era of the mitochondrial calcium uniporter. Nat Rev Mol Cell Biol 16, 545–553 (2015). [PubMed: 26285678]
6. Chen YW, Chen YF, Chen YT, Chiu WT, Shen MR, The STIM1-Orai1 pathway of store-operated Ca2+ entry controls the checkpoint in cell cycle G1/S transition. Sci Rep 6, 22142 (2016). [PubMed: 26917047]
7. Humeau J et al., Calcium signaling and cell cycle: Progression or death. Cell Calcium 70, 3–15 (2018). [PubMed: 28801101]
8. Skelding KA, Rostas JA, Verrills NM, Controlling the cell cycle: the role of calcium/calmodulin-stimulated protein kinases I and II. Cell Cycle 10, 631–639 (2011). [PubMed: 21301225]
9. Poburko D, Liao CH, van Breemen C, Demaurex N, Mitochondrial regulation of sarcoplasmic reticulum Ca2+ content in vascular smooth muscle cells. Circ Res 104, 104–112 (2009). [PubMed: 19023135]
10. Nemani N et al., MIRO-1 Determines Mitochondrial Shape Transition upon GPCR Activation and Ca. Cell Rep 23, 1005–1019 (2018). [PubMed: 29694881]
11. Montemurro C et al., Cell cycle-related metabolism and mitochondrial dynamics in a replication-competent pancreatic beta-cell line. Cell Cycle 16, 2086–2099 (2017). [PubMed: 28820316]
12. Pan X et al., The physiological role of mitochondrial calcium revealed by mice lacking the mitochondrial calcium uniporter. Nat Cell Biol 15, 1464–1472 (2013). [PubMed: 24212091]
13. Mitra K, Wunder C, Roysam B, Lin G, Lippincott-Schwartz J, A hyperfused mitochondrial state achieved at G1-S regulates cyclin E buildup and entry into S phase. Proc Natl Acad Sci U S A 106, 11960–11965 (2009). [PubMed: 19617534]
14. Han XJ et al., CaM kinase I alpha-induced phosphorylation of Drp1 regulates mitochondrial morphology. J Cell Biol 182, 573–585 (2008). [PubMed: 18695047]

15. Xu S et al., CaMKII induces permeability transition through Drp1 phosphorylation during chronic β-AR stimulation. Nat Commun 7, 13189 (2016). [PubMed: 27739424]
16. Cereghetti GM et al., Dephosphorylation by calcineurin regulates translocation of Drp1 to mitochondria. Proc Natl Acad Sci U S A 105, 15803–15808 (2008). [PubMed: 18838687]
17. Qi X, Disatnik MH, Shen N, Sobel RA, Mochly-Rosen D, Aberrant mitochondrial fission in neurons induced by protein kinase C{delta} under oxidative stress conditions in vivo. Mol Biol Cell 22, 256–265 (2011). [PubMed: 21119009]
18. Taguchi N, Ishihara N, Jofuku A, Oka T, Mihara K, Mitotic phosphorylation of dynamin-related GTPase Drp1 participates in mitochondrial fission. J Biol Chem 282, 11521–11529 (2007). [PubMed: 17301055]
19. Mallilankaraman K et al., MICU1 is an essential gatekeeper for MCU-mediated mitochondrial Ca(2+) uptake that regulates cell survival. Cell 151, 630–644 (2012). [PubMed: 23101630]
20. Labrousse AM, Zappaterra MD, Rube DA, van der Bliek AM, C. elegans dynamin-related protein DRP-1 controls severing of the mitochondrial outer membrane. Mol Cell 4, 815–826 (1999). [PubMed: 10619028]
21. Zaja I et al., Cdk1, PKCδ and calcineurin-mediated Drp1 pathway contributes to mitochondrial fission-induced cardiomyocyte death. Biochem Biophys Res Commun 453, 710–721 (2014). [PubMed: 25445585]
22. Chang BH, Mukherji S, Soderling TR, Characterization of a calmodulin kinase II inhibitor protein in brain. Proc Natl Acad Sci U S A 95, 10890–10895 (1998). [PubMed: 9724800]
23. Qi X, Qvit N, Su YC, Mochly-Rosen D, A novel Drp1 inhibitor diminishes aberrant mitochondrial fission and neurotoxicity. J Cell Sci 126, 789–802 (2013). [PubMed: 23239023]
24. Hall DD, Wu Y, Domann FE, Spitz DR, Anderson ME, Mitochondrial calcium uniporter activity is dispensable for MDA-MB-231 breast carcinoma cell survival. PLoS One 9, e96866 (2014). [PubMed: 24802861]
25. Marchi S et al., Downregulation of the mitochondrial calcium uniporter by cancer-related miR-25. Curr Biol 23, 58–63 (2013). [PubMed: 23246404]
26. Yu C et al., Mitochondrial calcium uniporter as a target of microRNA-340 and promoter of metastasis via enhancing the Warburg effect. Oncotarget 8, 83831–83844 (2017). [PubMed: 29137386]
27. Tosatto A et al., The mitochondrial calcium uniporter regulates breast cancer progression via HIF-1alpha. EMBO Mol Med 8, 569–585 (2016). [PubMed: 27138568]
28. Roderick HL, Cook SJ, Ca2+ signalling checkpoints in cancer: remodelling Ca2+ for cancer cell proliferation and survival. Nat Rev Cancer 8, 361–375 (2008). [PubMed: 18432251]
29. Motiani RK, Abdullaev IF, Trebak M, A novel native store-operated calcium channel encoded by Orai3: selective requirement of Orai3 versus Orai1 in estrogen receptor-positive versus estrogen receptor-negative breast cancer cells. J Biol Chem 285, 19173–19183 (2010). [PubMed: 20395295]
30. Legrand G et al., Ca2+ pools and cell growth. Evidence for sarcoendoplasmic Ca2+-ATPases 2B involvement in human prostate cancer cell growth control. J Biol Chem 276, 47608–47614 (2001). [PubMed: 11606580]
31. Doonan PJ et al., LETM1-dependent mitochondrial Ca2+ flux modulates cellular bioenergetics and proliferation. FASEB J 28, 4936–4949 (2014). [PubMed: 25077561]
32. Lou LL, Lloyd SJ, Schulman H, Activation of the multifunctional Ca2+/calmodulin-dependent protein kinase by autophosphorylation: ATP modulates production of an autonomous enzyme. Proc Natl Acad Sci U S A 83, 9497–9501 (1986). [PubMed: 3467320]
33. Patel R et al., Calcium/calmodulin-dependent phosphorylation and activation of human Cdc25-C at the G2/M phase transition in HeLa cells. J Biol Chem 274, 7958–7968 (1999). [PubMed: 10075693]
34. Rambold AS, Kostelecky B, Elia N, Lippincott-Schwartz J, Tubular network formation protects mitochondria from autophagosomal degradation during nutrient starvation. Proc Natl Acad Sci U S A 108, 10190–10195 (2011). [PubMed: 21646527]
35. Gomes LC, Scorrano L, Mitochondrial elongation during autophagy: a stereotypical response to survive in difficult times. Autophagy 7, 1251–1253 (2011). [PubMed: 21743300]

36. Patron M et al., MICU1 and MICU2 finely tune the mitochondrial Ca2+ uniporter by exerting opposite effects on MCU activity. Mol Cell 53, 726–737 (2014). [PubMed: 24560927]
37. Raffaello A et al., The mitochondrial calcium uniporter is a multimer that can include a dominant-negative pore-forming subunit. EMBO J 32, 2362–2376 (2013). [PubMed: 23900286]
38. Sancak Y et al., EMRE is an essential component of the mitochondrial calcium uniporter complex. Science 342, 1379–1382 (2013). [PubMed: 24231807]
39. Paillard M et al., Tissue-Specific Mitochondrial Decoding of Cytoplasmic Ca2+ Signals Is Controlled by the Stoichiometry of MICU1/2 and MCU. Cell Rep 18, 2291–2300 (2017). [PubMed: 28273446]
40. Tsai MF et al., Dual functions of a small regulatory subunit in the mitochondrial calcium uniporter complex. Elife 5, (2016).
41. Yamamoto T et al., Analysis of the structure and function of EMRE in a yeast expression system. Biochim Biophys Acta 1857, 831–839 (2016). [PubMed: 27001609]
42. Kamer KJ, Grabarek Z, Mootha VK, High-affinity cooperative Ca2+ binding by MICU1-MICU2 serves as an on-off switch for the uniporter. EMBO Rep 18, 1397–1411 (2017). [PubMed: 28615291]
43. Galiano RD, Michaels J, Dobryansky M, Levine JP, Gurtner GC, Quantitative and reproducible murine model of excisional wound healing. Wound Repair Regen 12, 485–492 (2004). [PubMed: 15260814]
44. Ray JL, Leach R, Herbert JM, Benson M, Isolation of vascular smooth muscle cells from a single murine aorta. Methods Cell Sci 23, 185–188 (2001). [PubMed: 12486328]
45. Westin ER et al., Telomere restoration and extension of proliferative lifespan in dyskeratosis congenita fibroblasts. Aging Cell 6, 383–394 (2007). [PubMed: 17381549]
46. Sebag SC et al., Mitochondrial CaMKII inhibition in airway epithelium protects against allergic asthma. JCI Insight 2, e88297 (2017). [PubMed: 28194433]
47. Cribbs JT, Strack S, Reversible phosphorylation of Drp1 by cyclic AMP-dependent protein kinase and calcineurin regulates mitochondrial fission and cell death. EMBO Rep 8, 939–944 (2007). [PubMed: 17721437]
48. Cribbs JT, Strack S, Functional characterization of phosphorylation sites in dynamin-related protein 1. Methods Enzymol 457, 231–253 (2009). [PubMed: 19426871]

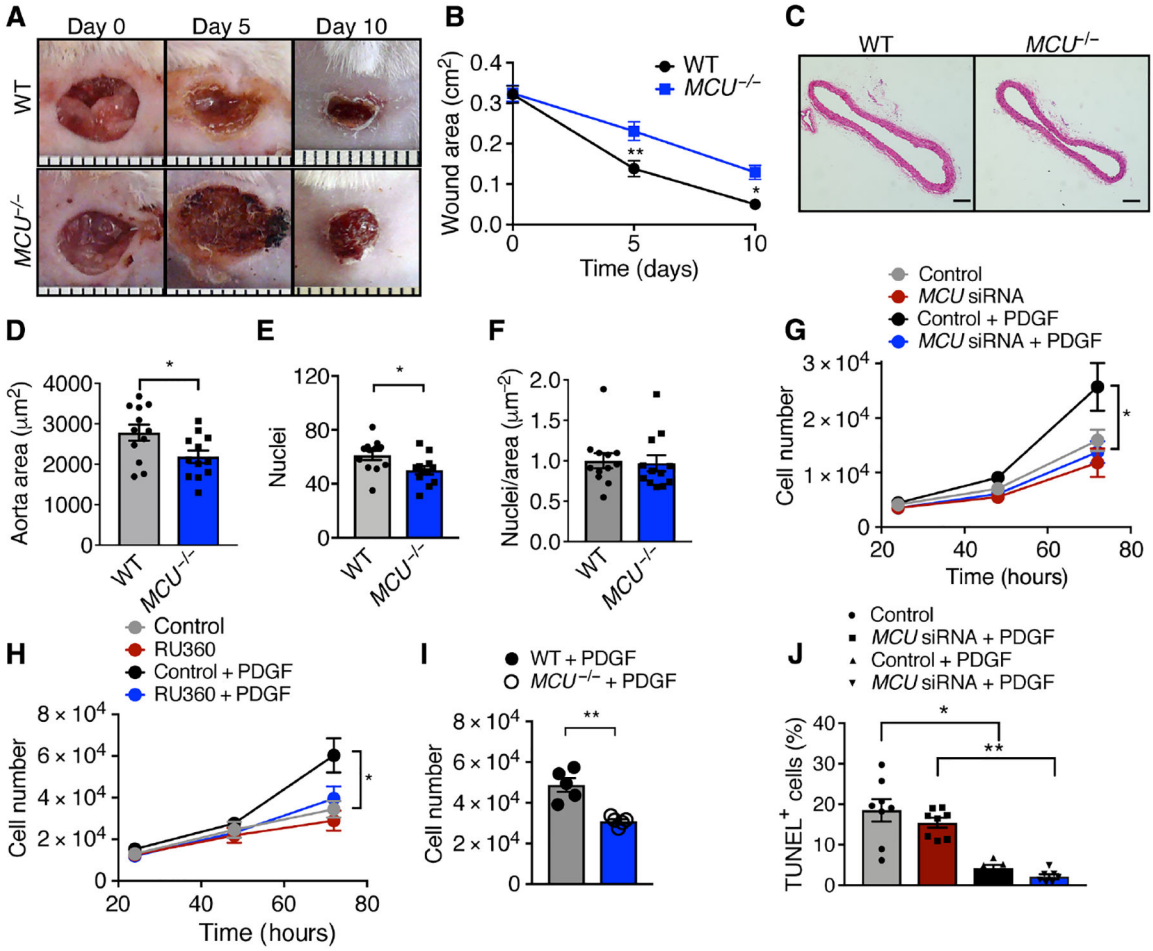

Figure 1. Deletion of MCU reduces cell proliferation in vivo and in vitro.

A) Interscapular wounds after skin punch in WT and *MCU*$^{-/-}$ mice. B) Quantification of wound area. n = 8 mice per genotype. C) H&E-stained cross sections of the descending aorta. Scale bar = 100 μm. D) Quantification of aortic medial cross-sectional areas. n = 12 mice per genotype. E) Quantification of cell nuclei in the aortic media. F) Ratio of nuclei per area, derived from E and D. G) Cell counts for cultured VSMCs transfected with MCU or scrambled siRNA in growth medium with 20 ng/mL PDGF. n = 9 independent experiments. H) Cell counts for VSMCs treated with the MCU inhibitor RU360 (100 nM) and/or PDGF. n = 8 independent experiments. I) Cell counts for skin fibroblasts from *MCU*$^{-/-}$ or WT mice at 72 h in growth medium with 20 ng/mL PDGF. n = 7 independent experiments. J) TUNEL-staining in VSMCs transfected with MCU or scrambled siRNA and treated with 20 ng/mL PDGF for 48 h. n = 6 independent experiments. * $p < 0.05$, ** $p < 0.001$ by 2-Way repeat measure ANOVA (B), Mann-Whitney test (D, F, I), two-tailed t-test (E), 1-way ANOVA at 48 h (G, H), Kruskal-Wallis test (J).

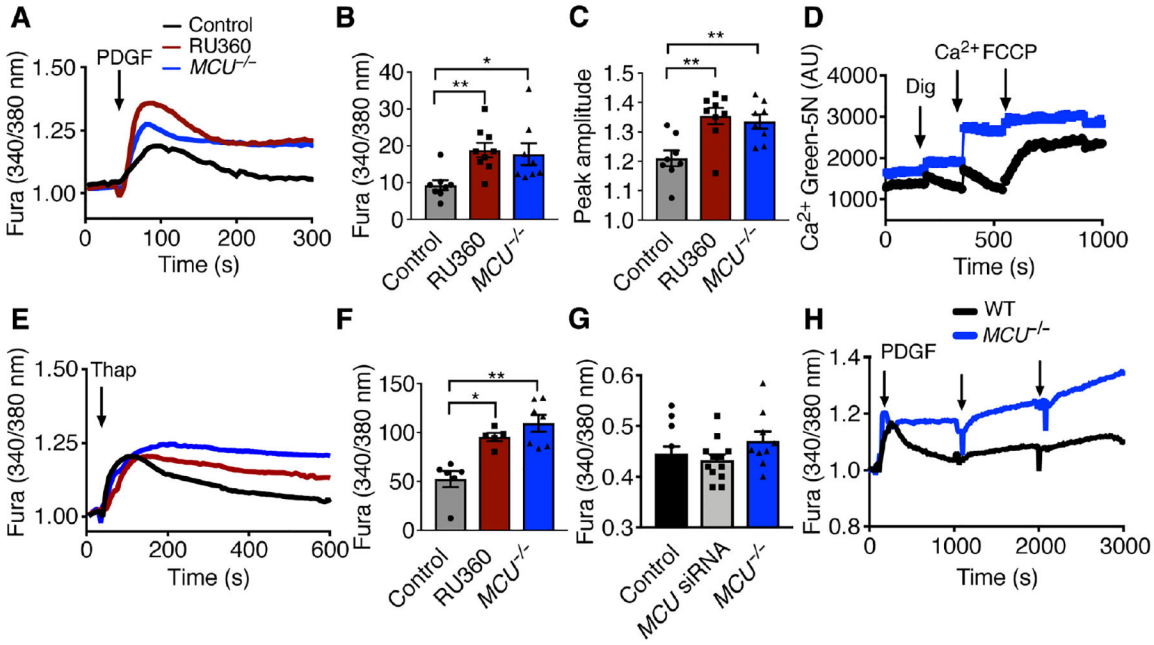

Figure 2. MCU activity is required for cytosolic Ca^{2+} clearance.

A) PDGF-evoked Ca^{2+} transients in WT and *MCU*$^{-/-}$ VSMCs and WT VSMCs pretreated with 100 nM RU360 for 16 h. (Arrow: addition of 10 nM PDGF). B) Area under the curve (AUC) for A. n = 5 independent experiments. C) Peak amplitude for A). n = 5 independent experiments with 8, 7 and 6 biological replicates for WT, *MCU*$^{-/-}$ and RU360 treatment). D) Mitochondrial Ca^{2+} uptake by Ca^{2+} Green 5N assay in WT and *MCU*$^{-/-}$ skin fibroblasts. Treatment with digitonin (Dig, 0.005%), Ca^{2+} (1 μM) and FCCP (25 μM). Representative of n = 2 independent experiments. E) Thapsigargin-induced Ca^{2+} transients in WT and *MCU*$^{-/-}$ VSMCs and WT VSMCs pretreated with 100 nM RU360. (Arrow: addition of 1 μM thapsigargin, Thap). F) Area under the curve in E. n = 5 independent experiment with 6, 7 and 5 replicates for WT, *MCU*$^{-/-}$ and RU360 treatment respectively. G) Quantification of baseline Fura signal in untreated WT VSMCs, WT VSMCs transfected with MCU siRNA, and *MCU*$^{-/-}$ VSMCs. n = 5 independent experiments with 12, 9, and 8 replicates for WT, MCU$^{-/-}$ and for WT VSMCs transfected with MCU siRNA respectively. * $p < 0.05$, ** $p < 0.01$compared to WT untreated by Kruskal-Willis test (B), 1-way ANOVA (C, F, G). H) Cytosolic Ca^{2+} levels by Fura recording in WT and *MCU*$^{-/-}$ VSMC after PDGF treatment (arrows) recorded over 3000 s. (n=4 independent experiments).

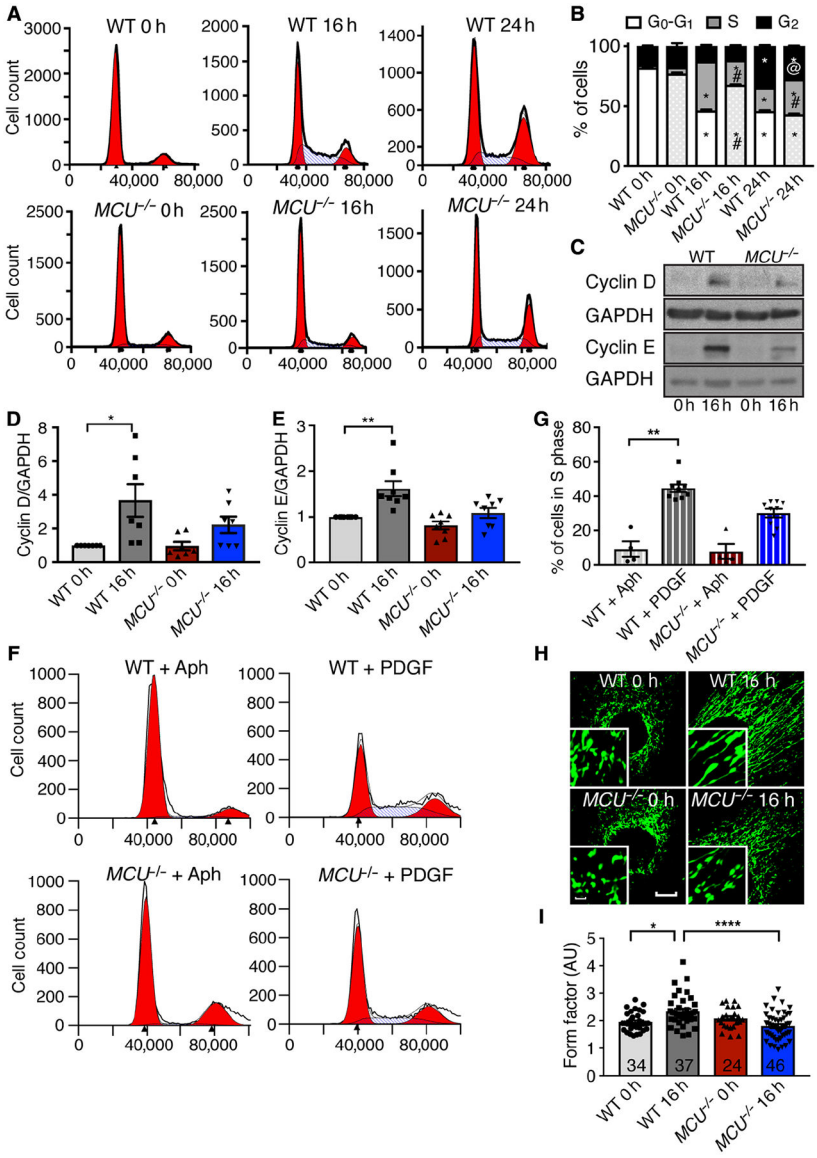

Figure 3. *MCU*$^{-/-}$ skin fibroblasts have blunted cell cycle progression from G1/S phase.

A) Representative FACS analysis for DNA content in synchronized/growth arrested WT and *MCU*$^{-/-}$ skin fibroblasts at 0 h, 16 h, and 24 h after release from arrest with 10% FBS + PDGF (10 ng/mL). B) Cell cycle phase distribution of fibroblasts from A). n=6 independent experiments with 11 replicates for WT and 12 for *MCU*$^{-/-}$, $^{\#}$ $p < 0.0001$ between genotypes, $^{@}$ $p < 0.005$ between genotypes by 2-way ANOVA. C) Immunoblots for cyclin D and cyclin E in synchronized/growth arrested skin fibroblasts (0 h) and at 16 h after 10% FBS + PDGF treatment (10 ng/mL). D) Quantification of cyclin D levels as in C). n=7 independent immunoblots. E) Quantification of cyclin E levels as in C). F) Progression to S phase after release from G1 arrest with Aphidicolin. n=4 independent experiments with total 7 replicates for WT and 8 for *MCU*$^{-/-}$. G) Quantification of F). n=4 independent experiments with total 7 replicates for WT and 8 for *MCU*$^{-/-}$. H) Confocal microscopy images of skin fibroblasts at baseline and 16 h after PDGF-induced cell cycle progression (mitoGFP, green). Scale bar =

20μm (larger image) or 5μm (inset). I) Mitochondrial form factor in skin fibroblasts in H). n = 5 independent experiments, number of cells of cells analyzed indicated in bars. * $p<0.05$, ** $p < 0.01$, **** $p < 0.001$ by Kruskal-Wallis test.

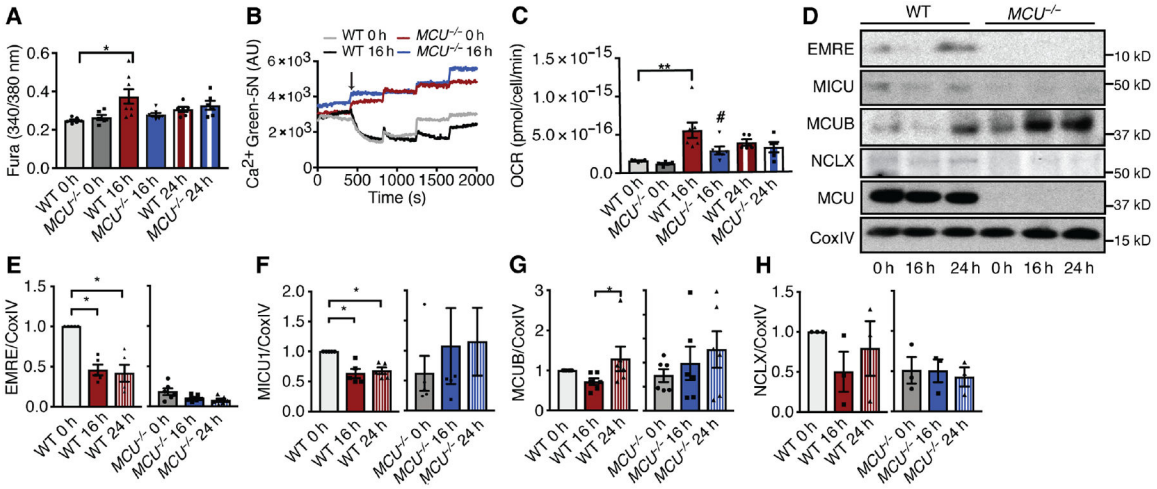

Figure 4. Dynamic regulation of oxygen consumption, mitochondrial and cytosolic Ca2+ uptake and MCU complex subunits during the cell cycle.

A) Fura recordings in skin fibroblasts at baseline and 16 h after serum/PDGF-induced cell cycle progression. n= 8 biological replicates for WT 16 h, 7 for *MCU*$^{-/-}$ 16 h, 6 for all other conditions. B) Ca^{2+} Green 5N assay in skin fibroblasts at baseline and 16 h after serum/PDGF-induced cell cycle progression. Treatment with digitonin (Dig, 0.005%, arrow), Ca^{2+} (1 μM, asterisks). n = 2 independent experiments. C) Oxygen consumption (OCR) by Clark electrode in skin fibroblasts at baseline and 16 h after PDGF-induced cell cycle progression. n= 7 biological replicates for WT 16 h, 6 for *MCU*$^{-/-}$ 16 h, 5 for all other conditions. D) Immunoblots for EMRE, MICU-1, MCUB, and NCLX at baseline and 16 h after serum/PDGF-induced cell cycle progression. E) Quantification of EMRE levels as in D). n = 6 independent experiments. F) Quantification of MICU-1 levels in D). n = 5 independent experiments. G) Quantification of MCUB levels as in D). n = 6 independent experiments. H) Quantification of NCLX levels as in D). n = 4 independent experiments. * $p<0.05$, ** $p < 0.01$ by Kruskal-Wallis test.

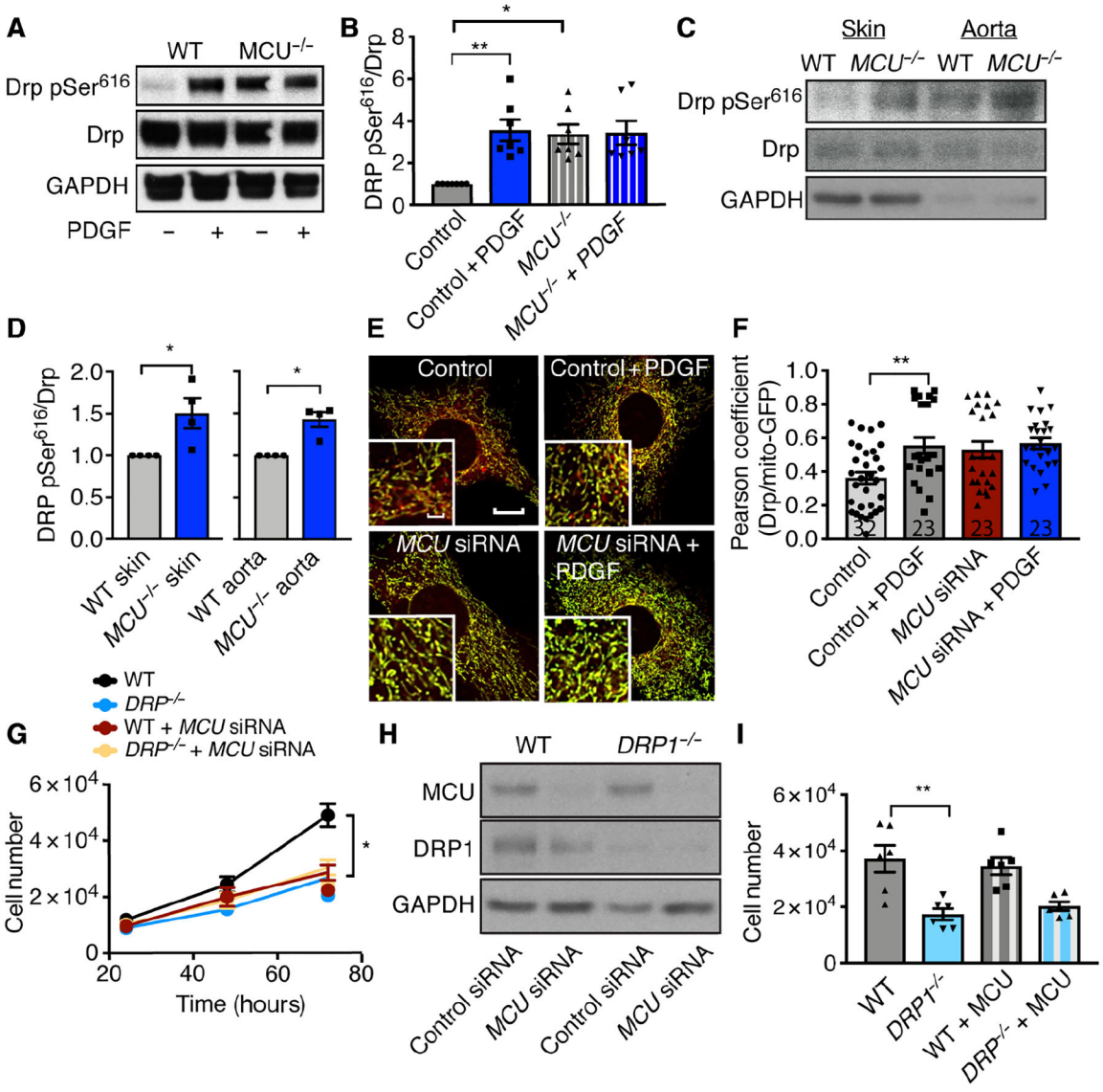

Figure 5. MCU deficiency increases Drp1 phosphorylation and mitochondrial fission.

A) Immunoblots for phosphorylated Drp1 (Drp1 pSer^{616}) and Drp1 in WT and *MCU*$^{-/-}$ VSMCs treated with PDGF for 20 min. B) Quantification of Drp1 phosphorylation normalized to Drp1 protein in PDGF-treated VSMCs as in A). n = 7 independent experiments. C) Immunoblots for Drp1 (Drp1 pSer^{616}) and Drp1 in tissue samples from the skin and aorta of WT and *MCU*$^{-/-}$ mice. D) Quantification of Drp1 phosphorylation at Ser^{616} normalized to Drp1 protein as in C). n = 4 independent experiments. E) Confocal microscopy images of mitochondria (mito-GFP, green) and Drp1 (red) in scrambled- or MCU siRNA-treated VSMCs before and at 40 min after PDGF treatment. Scale bars = 5 μm (inset) or 20 μm (larger image). F) Quantification of the co-localization of Drp1 and mito-GFP by Pearson Coefficient. n = 4 independent experiments, number of cells of cells analyzed indicated in bars. G) Cell counts *for Drp1*$^{-/-}$ embryonic fibroblasts transfected with MCU or scrambled siRNA and treated with growth medium with 10 ng/mL PDGF. n = 9 independent experiments. H) Immunoblots for MCU in *Drp1*$^{-/-}$ embryonic fibroblasts

transfected with MCU or scrambled siRNA as in G). n = 7 independent experiments. I) Cell counts in *Drp1*$^{-/-}$ embryonic fibroblasts with adenoviral overexpression of MCU for 48 h before culture in growth medium for 72 h. n = 6 independent experiments. * $p < 0.05$, ** $p < 0.01$ by Mann-Whitney test (D), Kruskal-Wallis test (B, F, I), Kruskal-Wallis test at 48 h (G).

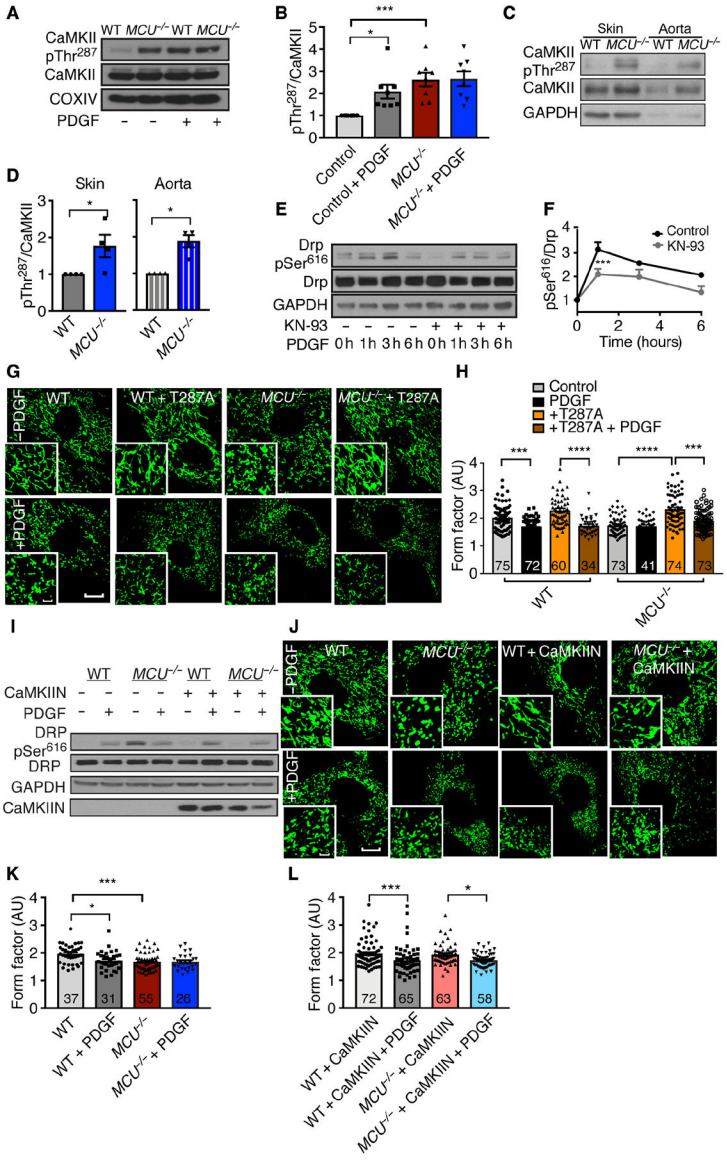

Figure 6. Cytosolic CaMKII is activated and controls mitochondrial fission when MCU is deleted.

A) Immunoblots for active CaMKII (CaMKII pThr^{287}) and CaMKII in WT and *MCU*$^{-/-}$ VSMCs treated with PDGF for 20 min. B) Quantification of CaMKII phosphorylation at Thr^{287} normalized to CaMKII protein in PDGF-treated WT and *MCU*$^{-/-}$ VSMCs as in A). n = 8 independent experiments. C) Immunoblots for phosphorylated CaMKII (CaMKII pThr^{287}) and CaMKII in tissue samples from the skin and aorta of WT and *MCU*$^{-/-}$ mice. D) Quantification of CaMKII phosphorylation at Thr^{287} normalized to CaMKII protein in the skin and aorta as in C). n = 4 independent experiments. E) Immunoblots for phosphorylated Drp1 (Drp1 pSer^{616}) and Drp1 protein in WT VSMCs treated with 30 μM KN-93 for 30 min before addition of PDGF. F) Quantification of Drp1 phosphorylation at Ser^{616} normalized to Drp1 protein in E). n = 3 independent experiments. G) Confocal microscopic images of mitochondria (mito-GFP, green) in WT and *MCU*$^{-/-}$ VSMCs after adenoviral overexpression of inactive CaMKII (CaMKII T287A) for 48 h, followed by

treatment with PDGF or control for 20 min. Scale bar = 20μm or 5 μm (inset). H) Quantification of form factor in WT and *MCU*$^{-/-}$ VSMCs with overexpression of CaMKII T287A or control in G). n = 5 independent experiments, number of cells analyzed indicated in bars. I) Immunoblots for phosphorylated, active Drp1 (Drp pSer^{616}), and Drp1 protein in WT and *MCU*$^{-/-}$ VSMCs with overexpression of CaMKIIN or control for 48 h followed by treatment with PDGF or control for 20 min. n = 2 independent experiments. J) Confocal microscopic images of mitochondria (mito-GFP, green) in WT and *MCU*$^{-/-}$ VSMCs after adenoviral overexpression of CaMKIIN for 48 h and treatment with PDGF or control for 20 min. Scale bar= 20 μm (larger image) or 5 μm (inset). K) Quantification of form factor in WT and *MCU*$^{-/-}$ VSMCs as in J). L) Quantification of form factor in WT and *MCU*$^{-/-}$ VSMCs with overexpression of CaMKIIN as in J). n = 5 independent experiments, number of cells analyzed indicated in bars. C, D) * $p < 0.05$, ** $p < 0.01$, *** $p < 0.005$, **** $p < 0.001$ by Kruskal-Wallis test (B, H, K, L), Mann-Whitney test (D) or 2-way repeat measure ANOVA (F).

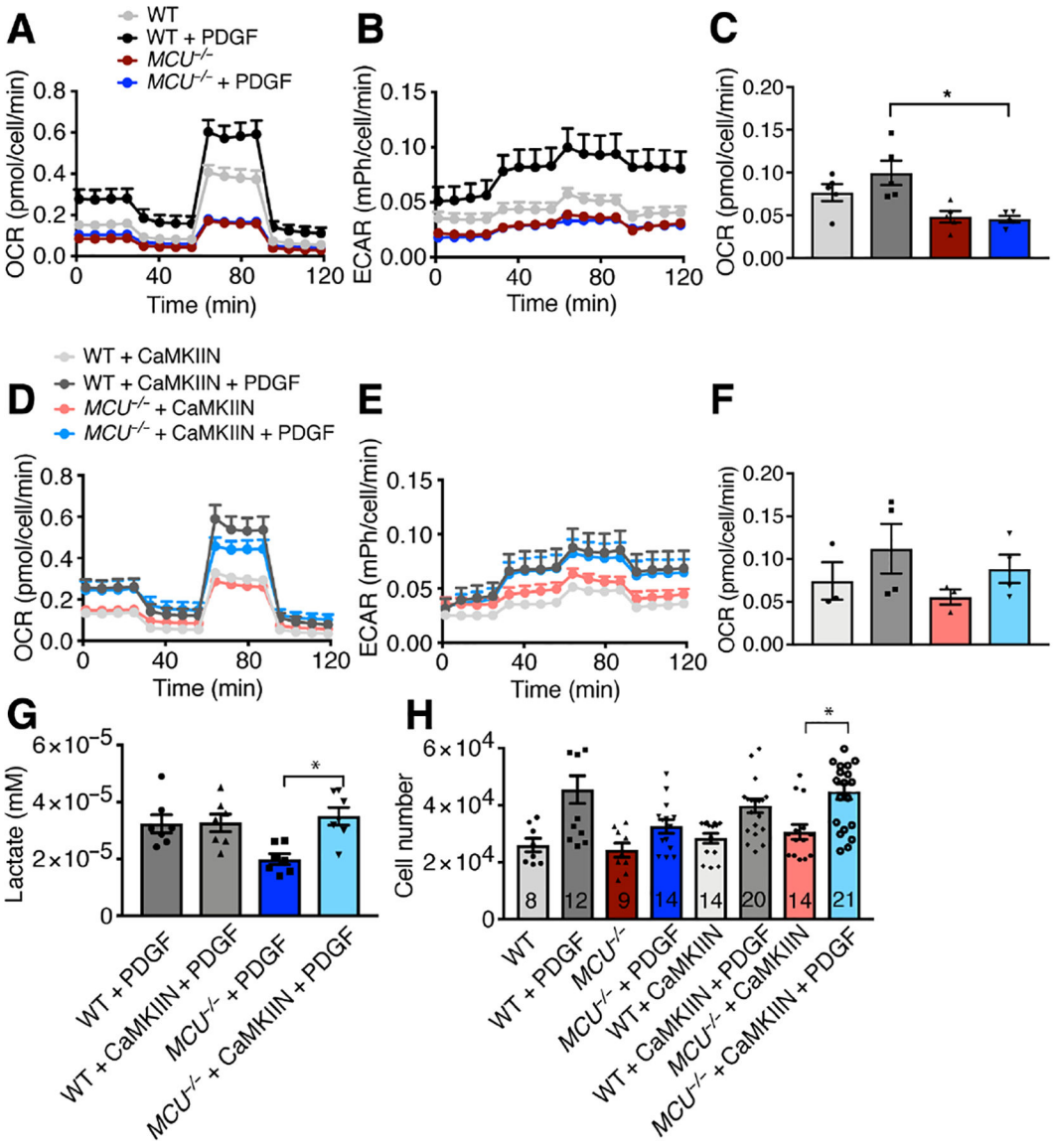

Figure 7. Cytosolic CaMKII inhibition in *MCU*$^{-/-}$ VSMCs rescues mitochondrial dynamics and cell proliferation.

A) Oxygen consumption rate (OCR) in WT and *MCU*$^{-/-}$ VSMCs after treatment with PDGF (20 ng/mL for 1 h) with sequential addition of oligomycin (Oligo, 1 μM), FCCP (1.5 μM), and rotenone/antimycin (2 μM). B) Extracellular acidification rate (ECAR) in WT and *MCU*$^{-/-}$ VSMCs after treatment with PDGF (20 ng/mL for 1 h). n = 5 independent experiments for A-C. C) Quantification of OCR for mitochondrial respiration calculated as Baseline OCR – OCR after oligomycin. D) OCR in WT and *MCU*$^{-/-}$ VSMCs with adenoviral overexpression of CaMKIIN after treatment with PDGF (20 ng/mL for 1 h). n = 3 independent experiments for control, 4 for independent experiments for PDGF treatment in D-F. E) ECAR in WT and *MCU*$^{-/-}$ VSMCs with adenoviral overexpression of CaMKIIN after treatment with PDGF (20 ng/mL for 1 h). F) Quantification of OCR for mitochondrial respiration calculated as baseline OCR – OCR after oligomycin. G) Lactate concentration in WT and *MCU*$^{-/-}$ VSMCs after adenoviral overexpression of CaMKIIN, serum starvation for

24 h, followed by treatment with growth medium containing PDGF for 24 h. n = 7 independent experiments. H) Number of WT and $MCU^{-/-}$ VSMCs with overexpression of CaMKIIN and control at 72 h after PDGF treatment or control. n = 6 independent experiments. Number of biological replicates indicated in bars. * $p < 0.05$ by Kruskal-Wallis test (C, F, G, H).

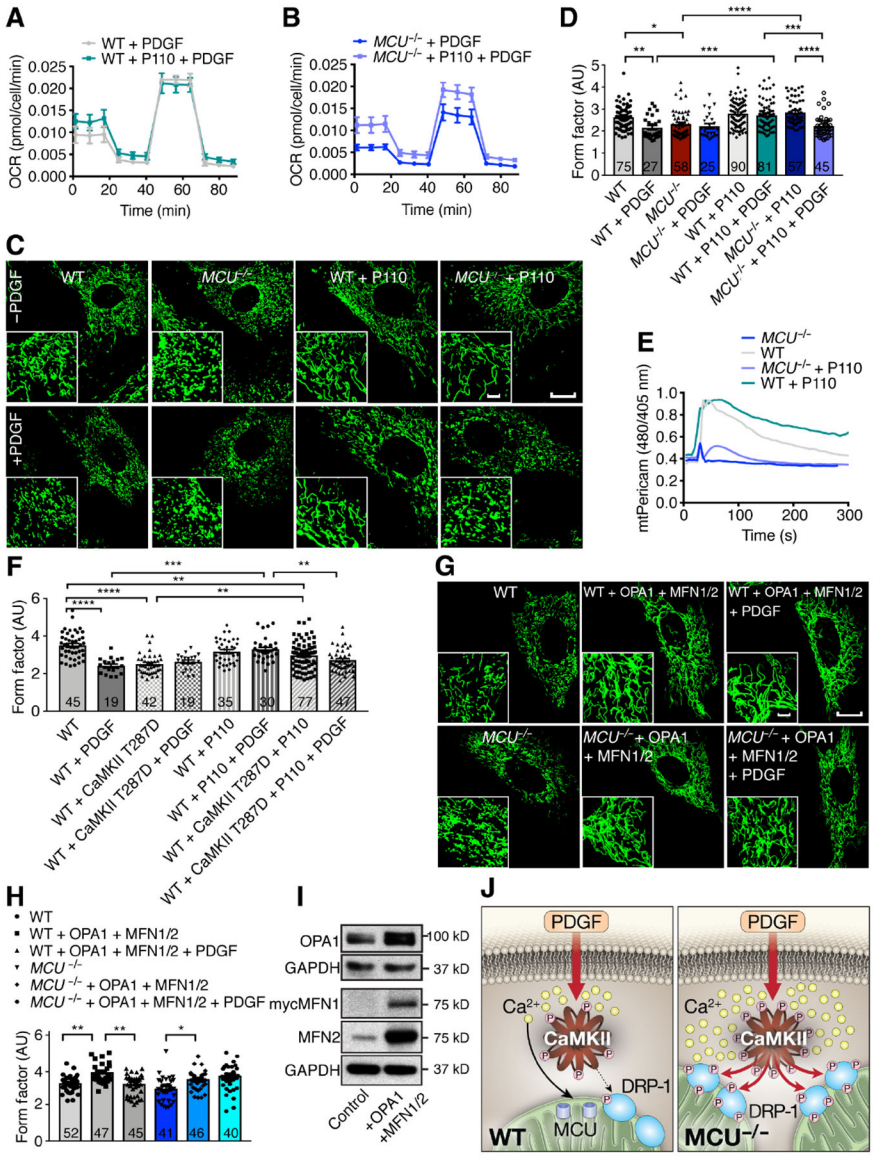

Figure 8. Inhibition of mitochondrial fission in *MCU*$^{-/-}$ VSMCs augments mitochondrial Ca^{2+} uptake, dynamics, and respiration.

A) Oxygen consumption rate (OCR) in WT VSMCs after treatment with P110 (2 μM for 16 h) and PDGF (20 ng/ml for 1 h). n = 3 independent experiments. B) OCR in *MCU*$^{-/-}$ VSMCs after treatment with P110 and PDGF. n=3 independent experiments. C) Confocal microscopic images of mitochondria (mito-GFP, green) in WT and *MCU*$^{-/-}$ VSMCs after treatment with P110 for 16 h and PDGF or control for 20 min. Scale bar = 20 μm (larger image) or 5 μm (inset). D) Summary histogram of form factor in control WT and *MCU*$^{-/-}$ VSMCs in D). Number of cells analyzed in 3 independent experiments indicated in bars. E) Average tracing of mitochondrial Ca^{2+} by mtPericam in WT or *MCU*$^{-/-}$ VSMCs after treatment with P110 (2 μM) for 16 h. Arrow indicates addition of PDGF (20 ng/ml). n = 3 independent experiments. F) Summary histogram of form factor in control WT VSMCs with adenoviral overexpression of constitutively active CaMKII (CaMKII T287D, MOI 100) or control. Samples pretreated with P110 as indicated. n = 3 experiments, number of cells

analyzed indicated in bars. G) Confocal microscopic images of mitochondria (mito-GFP, green) in WT and *MCU*$^{-/-}$ VSMCs after overexpression of OPA1 and MFN1/2 at the baseline and after PDGF treatment. Scale bar = 20 μm (larger image) or 5 μm (inset). H) Summary histogram of form factor in baseline WT and *MCU*$^{-/-}$ before and after overexpression of OPA1 and MFN1/2 before and after PDGF treatment. n = 3 independent experiments, number of cells analyzed indicated in bars. I) Immunoblots for OPA-1, Myc (myc-tagged MFN1), MFN2 and GAPDH in WT VSMCs and VSMCs with overexpression of OPA1 and MFN1/2. n = 2 independent experiments. J) Graphical summary, indicating that MCU deletion increases CaMKII activation, DRP1 phosphorylation and mitochondrial fission. * $p<0.05$, ** $p<0.01$, *** $p<0.005$, **** $p<0.001$ by Kruskal-Wallis test (D, F, H).